Drip paintings and fractal analysis

Katherine Jones-Smith,[1] Harsh Mathur,[1] and Lawrence M. Krauss[2]
[1]*Department of Physics, Case Western Reserve University, 10900 Euclid Avenue, Cleveland, Ohio 44106-7079, USA*
[2]*School of Earth and Space Exploration, Department of Physics and Beyond Center, Arizona State University, P.O. Box 871404, Tempe, Arizona 85287-1404, USA*

(Received 24 October 2007; revised manuscript received 25 November 2008; published 30 April 2009)

It has been claimed that fractal analysis can be applied to unambiguously characterize works of art such as the drip paintings of Jackson Pollock. This academic issue has become of more general interest following the recent discovery of a cache of disputed Pollock paintings. We definitively demonstrate here, by analyzing paintings by Pollock and others, that fractal criteria provide no information about artistic authenticity. This work has led us to a result in fractal analysis of more general scientific significance: we show that the statistics of the "covering staircase" (closely related to the box-counting staircase) provide a way to characterize geometry and distinguish fractals from Euclidean objects. Finally we present a discussion of the composite of two fractals, a problem that was first investigated by Muzy. We show that the composite is not generally scale invariant and that it exhibits complex multifractal scaling in the small distance asymptotic limit.

DOI: 10.1103/PhysRevE.79.046111 PACS number(s): 89.75.Da, 05.45.Df, 89.75.Kd, 95.75.Mn

I. INTRODUCTION

In 1999, a highly publicized work [1,2] applied fractal analysis to the works of Jackson Pollock. The recent discovery of a cache of approximately 25 paintings that may be the work of Pollock has motivated the application of these techniques [2–6] in order to determine authenticity of these paintings. However we argued in [7] that in fact Pollock's drip paintings cannot be usefully characterized as fractal, and that identical fractal characteristics can be trivially reproduced. In this work we analyze seven drip paintings (three by Pollock, two of the newly discovered paintings, and two commissioned works by local artists) and demonstrate conclusively that fractal criteria are not useful for authentication. In particular, we demonstrate both that known Pollock drip paintings and known non-Pollock paintings meet the claimed criteria at equal levels of significance. Our box-counting analysis led us to explore the asymptotics of overlapping fractals, which were found to be complex multifractals, and to discover an alternative way to use fractal analysis to characterize geometry.

The standard technique used to determine whether an image is fractal is to cover it with a grid of square boxes of size L and count the number of occupied boxes, N. For a fractal, $N \propto L^D$, where D is the fractal dimension and is noninteger. The box-counting curve (a plot of $\log N$ against $\log L$) is therefore a straight line with slope D. According to Taylor *et al.* [6] the box-counting curves of Pollock paintings meet the following criteria: (1) there are two fractal dimensions, $D_D < D_L$, where D_D is the fractal dimension for boxes smaller than a transition length L_T and D_L for boxes larger than L_T; (2) $L_T > 1.0$ cm; (3) the fits to the box-counting data are low noise with $\chi < 0.062$; and (4) for multicolored paintings each colored layer as well as the composite painting all satisfy criteria (1)–(3). Fractal authentication is based on the claim that all Pollock drip paintings satisfy these criteria. In addition it is also claimed that these characteristics are exclusive to Pollock, arising from his unique mastery of chaotic motion [2–6].

In previous work [7] we identified several problems with the fractal analysis of Taylor *et al.*: (i) an insufficient range of box sizes was used to establish fractal behavior, (ii) it is mathematically impossible for the visible portion of each layer and the composite to separately behave as fractals in a multilayered painting, and (iii) χ depends on the magnification factor used in box counting and is therefore not intrinsic to the image.

In this paper we first focus on whether, regardless of these issues, the box-counting curve can be used for authentication (Sec. II). In addition we investigate two problems in fractal mathematics motivated by our analysis of drip paintings but with results of broader significance. Whether fractal analysis allows authentication of drip paintings has immediate and significant financial implications in the art world, but the mathematical results presented here have more enduring scientific importance. In Sec. III we present an analysis of the noise inherent in the determination of a fractal dimension by looking at the statistics of a staircase function closely related to the box-counting staircase. We find that the statistics provide an alternative way to distinguish fractals from Euclidean objects. In Sec. IV we analyze overlapping fractals using Cantor dusts as concrete examples, a problem that has been studied earlier by Muzy [8].

II. ANALYSIS OF DRIP PAINTINGS

We first focus on whether, regardless of the aforementioned shortcomings, fractal analysis can be used for authentication. We begin our discussion of image analysis with the problem of color separation. A digital image in RGB mode describes each pixel by three numbers, its R (red), G (green), and B (blue) values, which lie in the range of 0–255. Naively one might expect individual colors to occupy distinct regions of RGB space, and to separate a particular color from the rest, one can simply define a median RGB value and collect the pixels that lie within a certain radius. This is precisely the color separation procedure used by Mureika *et al.* [9]. It is easy to implement but does not work particularly well [10], as illustrated in Fig. 1.

As color separation is a delicate task, we developed two independent techniques we call the Photoshop method and

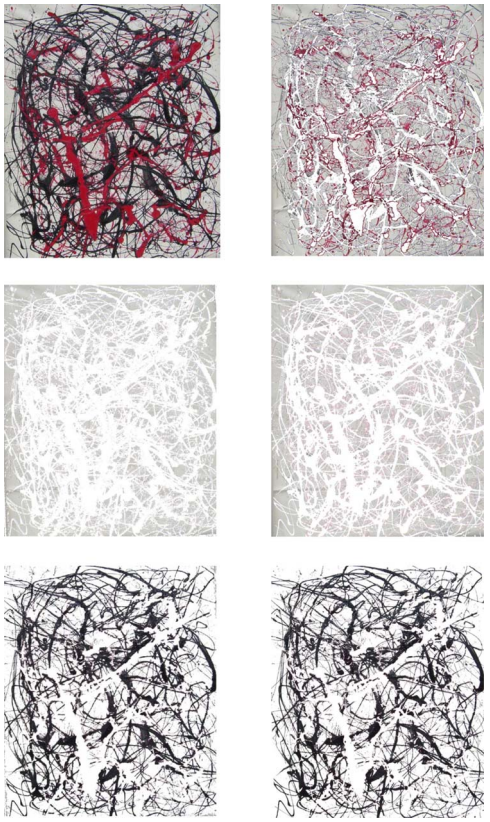

FIG. 1. (Color online) Color separation. *Composition with Red and Black* (top left) and its background layer (top right) as obtained with the color separation method of Mureika *et al.* [9]. The background layer for the same painting as obtained by the Photoshop (middle left) and RGB Mesh (middle right) methods. The black layer as obtained by Photoshop (bottom left) and RGB mesh (bottom right) methods.

the adaptive RGB mesh method; both are described in detail in Appendix A. Results from the two methods are in excellent agreement and are tabulated in Appendix B.

We now embark on a discussion of specific paintings, starting with three famous works by Pollock. A gallery of all paintings discussed below can be found in Appendix C. Their box-counting data are in Appendix B.

We chose to analyze *Free Form* (1946) because at one time it was listed by Taylor *et al.* [6] as one of the canonical Pollock paintings from which the fractal authentication criteria were developed [11]. Surprisingly, we find that *Free Form* does not conform perfectly to the fractal authentication criteria; specifically we find that for the composite image $L_T < 1.0$ cm. Although *Free Form* does not pass a rigorous application of the fractal authentication criteria, Ref. [6] describes a more relaxed procedure called force fitting. Force fitting imposes the constraint that $L_T > 1.0$ cm, thereby automatically satisfying authentication criterion (2). Thus authentication is reduced to checking that the other criteria are fulfilled. We find that force fitting *Free Form* does not significantly change D_D, D_L, or χ and these parameters do remain consistent with fractal authentication criteria. Thus adopting the more relaxed fractal authentication criterion, based solely on fractal analysis, one would conclude that *Free Form* is indeed authentic.

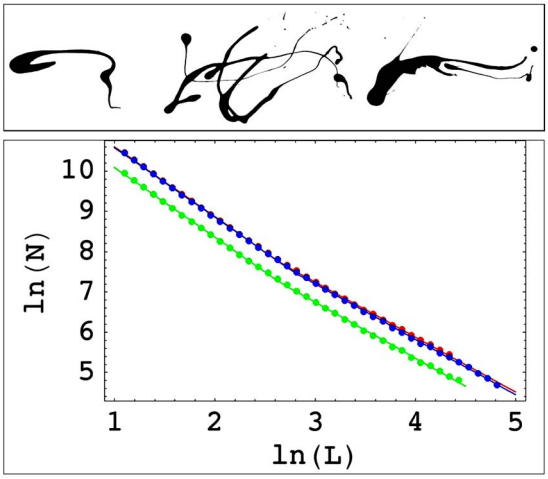

FIG. 2. (Color online) *Untitled* (ca. 1950) by Jackson Pollock, enamel on paper, 28.3×150.3 cm^2, Staatsgalerie, Stuttgart [12]. Box-counting curves for *Untitled* with color separation by the Photoshop method (red) and adaptive RGB mesh (blue) and cropped image (green, lower curve). The red and blue points lie on the upper curve and cannot be distinguished on a plot this size. Because of the awkward aspect ratio of this painting we were forced to scan it as two subimages which we then merged. The cropped image here corresponds to the larger of the two subimages. Pollock images are reproduced by permission ©2009 The Pollock-Krasner Foundation/ Artists Right Society (ARS), New York. Reproduction, including downloading of Pollocks works is prohibited by copyright laws and international conventions without the express written permission of ARS, New York.

No such stratagem avails for Pollock's *Untitled* (ca. 1950), shown in Fig. 2, which fails the fractal authentication test in a more spectacular way. Force fitting offers recourse for a painting with $L_T < 1.0$ cm, and χ can be decreased by trimming the range of box sizes; thus, anomalous dimensions $D_D > D_L$ are the clearest sign that a painting fails the fractal authentication test. It is in this respect that Pollock's *Untitled* (ca. 1950) fails. *The Wooden Horse: Number 10A, 1948* (1948) is another Pollock painting that unambiguously fails to satisfy the fractal authentication test. It has anomalous dimensions in two of six color layers (see Appendix B.) Thus, based solely on fractal analysis, one would conclude neither of these paintings (both of which are undisputed Pollock paintings) are authentic Pollocks.

Interestingly, two of the 25 extant paintings in the cache discovered by Alex Matter resemble *Free Form* and *Wooden Horse*. Taylor *et al.* analyzed six paintings from the Matter cache and found that none conformed to fractal authentication criteria [1]. We find that the fractal characteristics of the Matter paintings which resemble *Free Form* and *Wooden Horse* bear a striking similarity to the fractal characteristics of the two analogous Pollock paintings: the painting that resembles *Free Form* meets all the fractal authentication criteria provided we force fit the composite layer, and the painting that resembles *Wooden Horse* fails unambiguously by having anomalous dimensions in two out of six layers.

In [7] we demonstrated that crude drawings such as *Untitled 5* would be mistaken for authentic Pollocks by a com-

puter using fractal analysis for authentication. Although *Untitled 5* seriously undermined fractal authentication, it remained to show that actual drip paintings that are unquestionably not by Pollock too can satisfy the fractal authentication criteria; it is this step of the argument we now present. The artists we commissioned, Alexandra Ash and Michael Hallen, studied Pollock's technique and rendered nine drip paintings. Of these we have so far analyzed two paintings chosen for the relative ease with which they could be color separated. Both paintings satisfy all fractal authentication criteria comfortably, even without the force fitting required for *Free Form* (see Appendix B for results).

According to Taylor *et al.* [6] the fractal dimension on short length scales D_D increased during the course of Pollock's career so steadily that it may be possible to date a painting by its D_D value. The high D_D values we obtain for *Free Form* are more appropriate for a late period Pollock and are therefore not consistent with the claimed trend. Parenthetically we note that if we took this trend seriously we would identify the paintings of Ash and Hallen too as Pollock works from the late period of 1948–1952. Taylor *et al.* asserted that D_D and the small-scale structure result from the interaction of paint with the canvas to which it is applied. Presumably the value of D_D should then be affected by the porosity of the surface to which paint is applied. It is therefore surprising that Taylor *et al.* did not appear to have considered the effect on D_D that might result from the use of different materials. Although the best known works of Pollock are oil on canvas, he had a substantial body of work on paper [e.g., *Untitled* (1950)] and other materials (see, for example, [12]). In particular the canonical Pollock paintings of Taylor *et al.*, which they treated as a single homogeneous group, included both paintings on canvas and paintings on paper.

Finally we would like to comment on a feature of our data, namely, that a small number of the fractal dimensions we tabulate in Appendix B are found to be slightly greater than 2. For an ideal planar fractal the exact fractal dimension must be less than 2. But even for an ideal fractal, due to inevitable measurement errors, it is entirely possible to obtain a measured dimension slightly greater than 2 as explained below. Furthermore it must be remembered that the paintings we are analyzing are not ideal fractals.

The sources of uncertainty in the determination of fractal dimension D are (1) the box counts are discrete and deviate from a smooth fit through the box-counting curve, (2) round-off errors associated with digital blurring of the image, and (3) offset errors associated with a mismatch between the size of the boxes and the canvas [13]. Thus it is reasonable to expect that (a) the measured D would deviate slightly from the true ideal value; (b) as the range of box sizes measured is increased, the deviation from the true value should decrease; and (c) if the true fractal dimension is close to 2, we may obtain a dimension slightly greater than 2. For a more complete discussion of this topic we direct the reader to Ref. [14].

Note that a measured $D>2$ does not imply that boxes are overcounted. We have verified in cases where $D>2$ that the number of filled boxes returned by our box counter never exceeds the total number of boxes. Indeed by itself, the constraint that the filled boxes must be fewer in number than the total number of boxes does not require that the local slope of the box-counting curve has to be less than 2.

III. COUNTING STATISTICS

A. Overview

The box-counting curve is a staircase function because the number of filled boxes is an integer that increases monotonically as the box size is reduced. Staircase functions abound in mathematics and physics, e.g., $\Pi(x)$, the number of primes less than x [15]; $N(E)$, quantum energy levels less than E [16]; and $n(s)$, zeta function zeros whose imaginary part lies between zero and s [16]. In all these cases there has been a concerted effort to determine a smooth fit through the staircase as well as to characterize the deviations of the staircase from this smooth fit. For example, Gauss found a smooth asymptotic fit to $\Pi(x)$. The smooth form of $N(E)$ is basic to statistical mechanics. The deviations from regularity of $N(E)$ show remarkable universal behavior encapsulated by random-matrix theory. The deviation statistics of $n(s)$ are the subject of a conjecture, ancillary to the Riemann hypothesis, due to Dyson and Montgomery. By contrast, hitherto in fractal analysis the focus has been on finding a smooth power law fit to the staircase and extracting the exponent (the fractal dimension); we now study the deviations from regularity.

For simplicity, instead of the box-counting dimension we analyze a closely related variant [17], the covering dimension. Here the staircase $N(\varepsilon)$ is the number of intervals of size ε needed to cover the fractal. We first study a unit line segment for which $N(\varepsilon)\approx 1/\varepsilon$, corresponding to a covering dimension of 1. Consider the sequence of interval sizes $\varepsilon_n \equiv \varepsilon_0/C^n$, where $n=1,\ldots,M$. Here ε_0 is the largest interval size and C is the reduction factor. We define $\chi_n \equiv N(\varepsilon_n) - 1/\varepsilon_n$ as the deviation of the exact counting staircase from the smooth fit. It is easy to show that as $M\to\infty$, χ^2 (the mean value of χ_n^2) vanishes (Sec. III B below). Thus the counting curves of line segments are essentially noiseless. Similar analysis for the middle third Cantor dust shows that the deviates are uniformly distributed over a finite interval and have a nonzero mean-square value (Sec. III C below). Thus the fractal counting curve of the 1/3 dust is intrinsically noisy. Intuitively we can understand that Euclidean objects would be noiseless because the deviations from regular behavior originate at boundary points. A Euclidean segment has only two boundary points; fractals have an infinite number. We conjecture that counting curves are generically noiseless for Euclidean objects whereas they have well-defined deviate statistics and mean-squared deviation for fractals. Like simple random number sequences [18], the successive deviates for the 1/3 dust are given by a formula that involves modular arithmetic. The 1/3 dust deviates are highly correlated but it is tantalizing to speculate that there might be other fractals whose counting curves could serve as pseudorandom number sources.

Finally, we briefly consider the implications of these findings for paintings. For fractals χ^2 is pseudorandom and for generic images it may be C dependent; hence, the use of χ^2 as a characteristic of paintings advocated in Ref. [6] is inap-

propriate. Taylor *et al.* [6] suggested that Pollock's works are high-quality fractals because they have small χ^2 values. Our analysis shows that it is in fact Euclidean objects that have low χ^2.

B. Line segment

$N(\epsilon)$ is the smallest number of segments required to cover a unit line segment [17]. Evidently

$$N(\epsilon) = \mathrm{R}\left(\frac{1}{\epsilon}\right), \tag{1}$$

where $\mathrm{R}(x)$ is the smallest integer that is greater than or equal to x. In other words R rounds up its argument. $N_{\mathrm{smooth}}(\epsilon)=1/\epsilon$ is a smooth fit through this counting staircase. From the definition

$$\chi(\epsilon) = \ln N(\epsilon) - \ln N_{\mathrm{smooth}}(\epsilon) \tag{2}$$

and Eq. (1) it is easy to see that for small ϵ

$$\chi(\epsilon) = \epsilon\Delta(\epsilon). \tag{3}$$

Here $\Delta(\epsilon)=\mathrm{R}(1/\epsilon)-1/\epsilon$ lies between 0 and 1 since it represents the amount of round up.

We now sample the counting curve at a sequence of interval sizes $\epsilon_n=\epsilon_0/C^n$, where $C>1$ is a reduction factor, ϵ_0 is the largest interval size considered, and $n=0,1,2,\ldots,M-1$. The quantities of interest are $\chi_n=\chi(\epsilon_n)$, the deviations of the counting curve from the smooth fit at the sampled interval sizes. As usual the mean-square deviation is given by

$$\chi^2 = \frac{1}{M}\sum_{n=0}^{M-1}\chi_n^2. \tag{4}$$

It is easy to derive the bound

$$\chi^2 \leq \frac{\epsilon_0^2}{M}\frac{1}{1-1/C^2} \tag{5}$$

revealing that $\chi^2\to 0$ as $M\to\infty$. Thus Euclidean staircases are essentially noiseless.

C. Cantor dust

The analysis of the middle third Cantor dust proceeds exactly in parallel to the Euclidean line segment. The exact staircase function is given by

$$N(\epsilon) = 2^{n(\epsilon)},$$

$$n(\epsilon) = \mathrm{R}\left[\frac{\ln(1/\epsilon)}{\ln 3}\right]. \tag{6}$$

$N_{\mathrm{smooth}}=1/\epsilon^{D_{1/3}}$ is a smooth fit through this staircase where $D_{1/3}=\ln 2/\ln 3$ is the fractal dimension of the middle third dust. From the definition of $\chi(\epsilon)$ [Eq. (2)] and the exact staircase [Eq. (6)] it follows that

$$\chi(\epsilon) = \ln 2\left(\mathrm{R}\left[\frac{\ln(1/\epsilon)}{\ln 3}\right] - \frac{\ln(1/\epsilon)}{\ln 3}\right). \tag{7}$$

By sampling the counting curve in the usual way we obtain the sequence of deviates

$$\chi_n = \ln 2\left(\mathrm{R}\left[\frac{n\ln C}{\ln 3} - \frac{\ln\epsilon_0}{\ln 3}\right] - \left[\frac{n\ln C}{\ln 3} - \frac{\ln\epsilon_0}{\ln 3}\right]\right). \tag{8}$$

This leads us to contemplate expressions of the form

$$\xi_n = \mathrm{R}(an+b) - (an+b). \tag{9}$$

Let us make the rational choice $a=p/q$ where, without further loss of generality, we may take p and q to be coprime and $p<q$. From Eq. (9) it is easy to see that ξ_n is a uniformly spaced sequence of q points on the unit interval. Thus the χ_n's are seen to be uniformly distributed and highly correlated.

With suitable rescaling Eq. (9) may be written in the form $I_{n+1}=(\alpha n+\gamma)(\mathrm{mod}\ m)$, where $I_n=q\xi_n$ and α, γ, and m are suitable constants. This form is very close to a common random number generator $I_{n+1}=(\alpha I_n+\gamma)(\mathrm{mod}\ m)$ [18]. An interesting question raised by this similarity, one that we leave open, is whether there is a deterministic fractal whose counting staircase generates an acceptable pseudorandom sequence.

IV. ASYMPTOTIC SCALING BEHAVIOR OF FRACTAL COMPOSITES

A. Overview

In this section we consider the asymptotic scaling behavior of the composites of ideal fractals using Cantor dusts as concrete examples. Multicolored paintings provide a natural motivation to consider this problem but in fact we have learned that this problem has been formulated and studied independently and much earlier by Muzy [8]. Here we present an alternative analysis of this problem; our discussion is entirely self-contained.

For definiteness consider the asymptotic scaling behavior of the union of a middle 1/3 Cantor dust (dimension $D_{1/3}=0.6309\ldots$) and the 3/9 dust (dimension $D_{3/9}=0.5$) (see Ref. [7] and below). The 1/3 dust is iterated $2\Lambda_2$ times; the 3/9 dust, Λ_1 times. The geometry of the union is controlled by $\lambda=\frac{\Lambda_2}{\Lambda_1}$. These dusts are ideal fractals since the range over which fractal behavior is seen can be made arbitrarily large. In previous work [7] we showed that the union is not fractal because its box-counting curve is not a simple power law except in the asymptotic limit of very small box sizes. In that limit, the number of boxes filled with 1/3 dust overwhelms the number filled with 3/9 dust because $D_{1/3}>D_{3/9}$. Thus the union behaves as a fractal with dimension $D_{1/3}$.

The full asymptotic complexity of the union is brought out by consideration of the spectrum of multifractal dimensions D_q. On small scales the 1/3 dust determines the fractal dimension D_0, but the 3/9 dust can control D_q for sufficiently large q. Figure 3 shows that, except in the trivial instances that one dust overwhelms the other, the union is not scale invariant over the same range as the constituent fractals. Moreover for fixed λ, varying q can produce a discontinuous jump in the dimension D_q. By contrast, for an ideal fractal D_q is independent of q. For generic multifractals D_q varies smoothly with q. Discontinuities in D_q are of great interest due to the thermodynamic analogy between multifractal di-

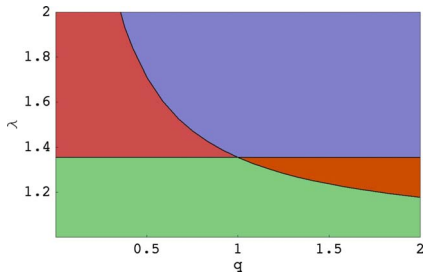

FIG. 3. (Color online) Phase diagram for overlapping Cantor dusts. A 1/3 Cantor dust is iterated $2\Lambda_2$ times and a 3/9 Cantor dust is iterated Λ_1 times. The geometry of their union is characterized by a single parameter $\lambda=\frac{\Lambda_2}{\Lambda_1}$. The behavior of the multifractal spectrum of dimensions D_q of the union is encapsulated by the phase diagram depicted here. In the green phase (lower left region) the 1/3 dust completely dominates and $D_q=D_{1/3}=0.6309$. Similarly in the blue phase (upper right region) the 3/9 dust dominates and $D_q=D_{3/9}=0.5$. But in the pink region (upper left) the 3/9 dust dominates on long length scales and the 1/3 on short scales; the effective dimension D_q crosses over from $D_{3/9}$ to $D_{1/3}$. In the orange region (middle sliver on the right) the crossover is from 3/9 to 1/3. If we focus on the shortest scales for a fixed $\lambda<\lambda_c=1.354\ldots$, D_q jumps from $D_{1/3}$ to $D_{3/9}$ as q is increased. Similarly for fixed $\lambda>\lambda_c$, the jump is from $D_{3/9}$ to $D_{1/3}$. Thus on the shortest scales the union of two fractals is revealed to be a complex multifractal. The vertical line $q=0$ corresponds to the ordinary fractal dimension. Along this line we find relatively trivial behavior: the 1/3 dust always dominates and the union behaves asymptotically as a fractal with dimension $D_{1/3}$.

mensions and phase transitions [19,20]. Thus the union is revealed to be a complex multifractal on the shortest length scales; details of the derivation are now presented in Secs. IV B and IV C below.

Let us briefly consider the relevance of this analysis to paintings. Taylor *et al.* [6] asserted that the composite of two colored layers is a fractal with a dimension that is different from either of its constituent layers. This assertion is mathematically impossible. It is presumably an artifact of fitting power-law behavior to data over a limited range.

B. Construction of Cantor dusts

The 1/3 dust [19] is constructed by starting with a unit line segment and removing the middle third. At the second iteration the middle third of the two surviving segments is removed; at the third iteration, the middle third of the four surviving segments. After Λ iterations the set consists of 2^Λ segments each of length $1/3^\Lambda$. This set behaves as a fractal on length scales between 1 and $1/3^\Lambda$. By increasing Λ we can make this range arbitrarily large, thus approaching a mathematical fractal.

There is a useful way to label segments using base 3 numbers. At the first iteration we label the left, middle, and right thirds of the initial unit segment as 0, 1, and 2, respectively. We then label the left, middle, and right thirds of the left third 00, 01, and 02, respectively. Proceeding in this way we see that after the second iteration the four segments that survive have the labels 00, 02, 20, and 22. After Λ iterations there are 3^Λ segments. The address of each segment is a base 3 number of Λ digits. The segments that survive are the ones that have only 0's and 2's in their base three addresses.

The 3/9 dust is constructed by starting with a unit line segment, dividing it into nine equal segments, and retaining only the first, fifth, and ninth segments [7]. At the second iteration the surviving segments are divided up into ninths and in each case only the first, fifth, and ninth subsegments are retained. After Λ iterations the set consists of 3^Λ segments each of length $1/9^\Lambda$. Segments in the 3/9 dust can be labeled by using base 9 numbers. For example, after the first iteration the segments that are retained are labeled 0, 4, and 8. After Λ iterations the segments will have labels that consist of base 9 numbers of Λ digits. The segments that belong to the 3/9 dust will have only 0's, 4's, and 8's in their address.

Another point of view on the 1/3 dust is that it is obtained by taking the unit segment, dividing it up into ninths, and retaining the first, third, seventh, and ninth segments. From this point of view, after 2Λ iterations the dust consists of 4^Λ segments each of length $1/9^\Lambda$. From this perspective segments can be labeled by base 9 numbers. For example, after the first iteration the four surviving segments are 0, 2, 6, and 8. After 2Λ iterations the segments will have labels that consist of base 9 numbers of Λ digits. The ones that belong to the 1/3 dust will have only 0's, 2's, 6's, and 8's in their address. This viewpoint on the 1/3 dust is useful when studying its union and intersection with the 3/9 dust.

C. Asymptotic analysis of overlapping fractals

1. Two Cantor dusts

First we summarize our results, then we outline their derivation. Consider the union of a 1/3 Cantor dust iterated $2\Lambda_2$ times and a 3/9 dust iterated Λ_1 times with $\lambda\equiv\Lambda_2/\Lambda_1\geq 1$. This construction results in 4^{Λ_2} segments each of length $1/9^{\Lambda_2}$ and $3^{\Lambda_1}-2^{\Lambda_1}$ segments each of length $1/9^{\Lambda_1}$. The total length of the resulting object is therefore

$$l_{\mathrm{tot}}=4^{\Lambda_2}\frac{1}{9^{\Lambda_2}}+(3^{\Lambda_1}-2^{\Lambda_1})\frac{1}{9^{\Lambda_1}}. \tag{10}$$

We suppose that the resulting object has unit mass and that the density (mass per unit length) is uniform and hence equal to $1/l_{\mathrm{tot}}$.

We now cover this object with boxes of size $\epsilon=1/9^\mu$, where $1\leq\mu\leq\Lambda_1$. It turns out that there are three classes of filled boxes. The number of boxes of each class and the mass contained within each box are given by

$$\begin{aligned} n_A&=2^\mu,\\ m_A&=[4^{\Lambda_2-\mu}/9^{\Lambda_2}+(3^{\Lambda_1-\mu}-2^{\Lambda_1-\mu})/9^{\Lambda_1}]/l_{\mathrm{tot}},\\ n_B&=4^\mu-2^\mu,\\ m_B&=[4^{\Lambda_2-\mu}/9^{\Lambda_2}]/l_{\mathrm{tot}},\\ n_C&=3^\mu-2^\mu,\\ m_C&=[3^{\Lambda_1-\mu}/9^{\Lambda_1}]/l_{\mathrm{tot}}. \end{aligned} \tag{11}$$

Instead of the number of filled boxes of size ϵ, in multifractal analysis [19] we consider the generalized box count $N(q,\epsilon)$ defined as

$$\ln N(q,\epsilon) = \frac{1}{1-q}\ln \sum_i m_i^q. \tag{12}$$

Here q is a continuous real parameter, m_i is the mass in the ith occupied box, and the sum is over all filled boxes. For multifractals it is expected that $N(q,\epsilon)$ will vary as a power of box size ϵ. Thus we may extract the multifractal spectrum of dimensions by computing

$$D_q = \lim_{\epsilon\to 0} \frac{\ln N(q,\epsilon)}{\ln(1/\epsilon)}. \tag{13}$$

Evidently $N(q,\epsilon)$ is equal to the number of filled boxes for $q=0$ and D_0 is just the ordinary fractal dimension. Making use of Eq. (11), it follows that for the overlapping Cantor dusts

$$N(q,\epsilon) = \frac{1}{1-q}\ln(n_A m_A^q + n_B m_B^q + n_C m_C^q). \tag{14}$$

Equation (14) is the central result of this section. It allows us to plot the generalized box-counting curve of the union of the Cantor dusts as well as to determine the asymptotic behavior.

The phase diagram for the overlapping Cantor dusts can be constructed by straightforward asymptotic analysis of Eq. (14). It is easy to argue that class B and class C boxes generally dominate the contribution of class A to the generalized box count. When class B dominates class C the generalized box count approaches that of a pure 1/3 dust; when class C dominates class B, it approaches that of a pure 3/9 dust. First consider the case $0<q<1$. In this case for $1<\lambda<\lambda_c$ the 1/3 dust dominates; for $\lambda>\lambda^+$ the 3/9 dust dominates. For $\lambda_c<\lambda<\lambda^+$ there is a crossover: the 3/9 dust dominates for $\mu<\mu_c$ and the 1/3 dust dominates for $\mu>\mu_c$. Here $\lambda_1=\ln 3/\ln(9/4)=1.354\ldots$, λ^+ is the curve defined by $\lambda^+=1+(\lambda_c-1)/q$, and μ_c is given by

$$\mu_c = \Lambda_1 \frac{q}{1-q}\frac{[\lambda\ln(9/4)-\ln 3]}{\ln(4/3)}. \tag{15}$$

Note that μ_c/Λ_1 varies from 0 to 1 as λ varies from λ_c to λ^+.

Similarly for $q>1$ we find that for $\lambda>\lambda_c$ the 3/9 dust dominates. For $\lambda^+>\lambda>1$ the 1/3 dust dominates. For $\lambda^+>\lambda>\lambda_c$ there is a crossover: the 1/3 dust dominates for $\mu<\mu_c$ and the 3/9 for $\mu>\mu_c$, where μ_c is given by Eq. (15).

Now we outline the derivation of these results. For simplicity we only consider the union of two Cantor dusts with $\Lambda_2=\Lambda_1=\Lambda$; the generalization is straightforward. We adopt the notation that $n=0$ or 8, $m=2$ or 6, $\nu=0$, 4, or 8, and $N=0$, 2, 6, or 8. After the first iteration of the 3/9 dust and the second iteration of the 1/3 dust the base 9 addresses of the surviving segments are 0, 2, 4, 6, and 8. In terms of the notation above the addresses are n_1, m_1, or 4. At the next iteration the possible addresses are n_1n_2; n_1m_2, m_1N_2; and n_1 4 or 4 ν_2. By working out a few iterations with this notation it is easy to deduce that once an m appears in an address the subsequent integers in the address must be Ns. Once a 4 appears, the subsequent integers are ν's. On the other hand, an n can be followed by n, m, or 4. Thus after Λ iterations the segments fall into three classes with binary addresses that (A) are composed entirely of n's, (B) include at least one m, and (C) include at least one 4. By induction we can show that $n_A=2^\Lambda$, $n_B=4^\Lambda-2^\Lambda$, and $n_C=3^\Lambda-2^\Lambda$. Since all segments are of length $1/9^\Lambda$ we can easily write down an expression for the total length of the object l_{tot} which is in agreement with Eq. (10).

Now suppose we cover the object with boxes of size $1/9^\mu$ where $\mu<\Lambda$. The boxes themselves fall into the three classes A, B, and C depending on their base 9 addresses. A class A box has only n's in its base 9 address. A segment that lies in a class A box has the same sequence of n's for the first μ digits of its base 9 address. The remaining $\Lambda-\mu$ digits may be n's, m's, or 4's. Thus the segments contained in a class A box effectively constitute the union of a 1/3 and 3/9 dust that is iterated $\Lambda-\mu$ times. Therefore it contains $4^{\Lambda-\mu}+3^{\Lambda-\mu}-2^{\Lambda-\mu}$ segments. Moreover, since the address of a class A box is a string of n's of length μ, evidently there are 2^μ class A boxes. In the same way we can show that there are $4^\mu-2^\mu$ boxes of class B and $3^\mu-2^\mu$ boxes of class C. The segments in a class B box have a base 9 address that coincides with that of the box for the first μ places. According to the rules above this is followed by a string of Ns of length $\Lambda-\mu$. Thus a class B box contains $4^{\Lambda-\mu}$ segments. Similarly a segment in a class C box has a base 9 binary address that coincides with that of the box for the first μ places. Thereafter it is a string of ν's of length $\Lambda-\mu$. Thus a class C box contains $3^{\Lambda-\mu}$ segments. With this we have derived all the information in Eq. (11) for the special case $\Lambda_1=\Lambda_2=\Lambda$. The derivation is readily generalized to the case $\Lambda_1\neq\Lambda_2$.

Note also that for this special case we have also shown that the number of filled boxes of size $1/9^\mu$ is $4^\mu+3^\mu-2^\mu$. This is the result plotted in Fig. 1 of Ref. [7] to illustrate that the box-counting curve for the union of two fractals is not a simple power law.

2. Euclidean island in sea of Cantor dust

We now briefly outline a second soluble example of the union of two objects with distinct fractal dimensions. The set we consider consists of a 1/3 dust that is initially iterated Λ_1 times. The segment to the extreme right (the Euclidean island) is now left fixed. The other surviving segments are further subdivided a further Λ_2 times to form a fine 1/3 dust. The Euclidean island has a length $1/3^{\Lambda_1}$. The dust consists of $2^{\Lambda_1+\Lambda_2}-2^{\Lambda_2}$ segments each of length $1/(3^{\Lambda_1+\Lambda_2})$. The total length of the object is therefore

$$l_{\text{tot}} = \frac{1}{3^{\Lambda_1}} + (2^{\Lambda_1+\Lambda_2}-2^{\Lambda_2})\frac{1}{3^{\Lambda_1+\Lambda_2}}. \tag{16}$$

Let us now cover the object with boxes of size $\epsilon=1/(3^{\Lambda_1+\mu})$, where $0\le\mu\le\Lambda_2$. The occupied boxes fall into class (A) that covers dust and class (B) that covers the Euclidean island. It is easy to see that

$$n_A = 2^{\Lambda_1+\mu}-2^\mu, \quad m_A = \frac{1}{l_{\text{tot}}}2^{\Lambda_2-\mu}\frac{1}{3^{\Lambda_1+\Lambda_2}},$$

$$n_B = 3^{\mu}, \quad m_B = \frac{1}{l_{\text{tot}}} \frac{1}{3^{\Lambda_1+\mu}}. \tag{17}$$

Thus the generalized box count defined in Eq. (12) is given by

$$\ln N(q,\epsilon) = \frac{1}{1-q} \ln(n_A m_A^q + n_B m_B^q). \tag{18}$$

Equation (18) is the main result of this section. It allows us to plot the generalized box-counting curve for this composite object as well as to analyze its asymptotic behavior.

The phase diagram implied by Eqs. (17) and (18) can be obtained by straightforward asymptotic analysis. The geometry of the union of the island and dust is controlled by a single parameter $\lambda \equiv \Lambda_1/\Lambda_2$. First consider $0 \le q < 1$. It is convenient to define $\lambda_0 = \ln(3/2)/\ln 2 = 0.584\,96\ldots$. Now for $\lambda < q\lambda_0$ the island dominates and the dimensions $D_q = 1$. For $\lambda > \lambda_0$ the dust dominates and the dimensions $D_q = D_{1/3}$, the fractal dimension of the 1/3 dust. For $q\lambda_0 < \lambda < \lambda_0$ the dust dominates for $\mu < \mu_0$, the island for $\mu > \mu_0$; the slope of the generalized box-counting curve crosses over from $D_{1/3}$ to 1. Here the crossover scale μ_0 is given by

$$\mu_0 = \Lambda_2 \frac{1}{1-q} \frac{\lambda - q\lambda_0}{\lambda_0}. \tag{19}$$

Now consider $q > 1$. In this case for $\lambda < \lambda_0$ the island dominates and the dimensions $D_q = 1$. For $\lambda > q\lambda_0$ the dust dominates and $D_q = D_{1/3}$. For $\lambda_0 < \lambda < q\lambda_0$ the island dominates for $\mu < \mu_0$ and the dust for $\mu > \mu_0$; the slope of the generalized box-counting curve crosses over from 1 to $D_{1/3}$. This information is encapsulated in the phase diagram shown in Fig. 4.

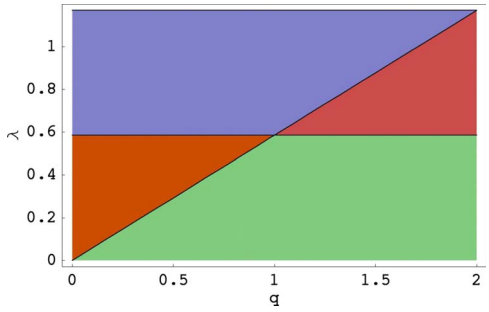

FIG. 4. (Color online) Phase diagram for Euclidean segment and Cantor dust. The geometry of the union of the two sets is controlled by a single parameter $\lambda = \Lambda_1/\Lambda_2$, where Λ_1 is the scale of the island and $\Lambda_1 + \Lambda_2$ of the dust as explained in the text. The diagram shows the behavior of the multifractal spectrum of dimensions D_q as a function of λ and q. In the green phase (lower right region) the island dominates completely and $D_q = 1$. Similarly in the blue phase (upper left region) the 1/3 dust dominates and $D_q = D_{1/3}$. But in the pink region (upper right region) the island dominates on long scales while the dust dominates on short scales; the effective dimension D_q crosses over from 1 to $D_{1/3}$. In the orange region (lower left) the dust dominates on long length scales and the island on short scales; the effective dimension D_q crosses over from $D_{1/3}$ to 1. If we fix λ, D_q jumps discontinuously as a function of q over an appropriate range of length scales. Thus the union of the two sets is a complex multifractal on these scales.

V. CONCLUSION

In summary, while in [7] we briefly described various shortcomings of fractal analysis as an authentication tool and identified a number of mathematical inconsistencies lurking in the mere application of fractal analysis to multicolored drip paintings, we have shown here that (i) amateur artists seeking to emulate Pollock's technique can successfully create paintings which possess the fractal signature said to be unique to Pollock and (ii) even authentic Pollock paintings fail to possess his fractal signature. Contrary to Taylor *et al.*, we also find at least one Matter painting possesses Pollock's fractal signature. Finally, our analysis presented a study of the statistics of counting staircases, a topic in fractal mathematics that invites much further exploration.

ACKNOWLEDGMENTS

We thank Alexandra Ash and Michael Hallen for rendering nine drip paintings, Ellen Landau and David Huse for discussions, and acknowledge support from the U.S. Department of Energy at Case Western Research University.

APPENDIX A: COLOR SEPARATION

In a digital image the color of each pixel is described by three numbers each of which lies in the range of 0–255 (its R, G, and B values). Thus color or RGB space may be viewed as a cube. Each pixel corresponds to a point inside this cube. Naively one might expect that pixels of the same color would clump together in color space and pixels of different colors would be well separated. But in fact human color perception is highly nonlinear: in some regions of color space a small variation in the RGB values can lead to a dramatic change in perceived color; in other regions, large variations in the RGB values correspond to essentially no change in the perceived color. Thus different colors form large almost interpenetrating regions in color space (see Fig. 5) and color separation is therefore a formidable task.

Consider separating a painting such as *Composition with*

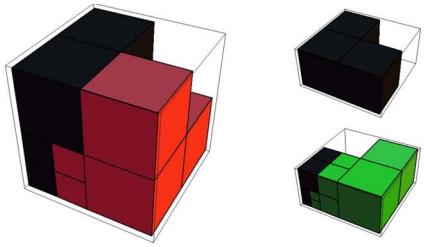

FIG. 5. (Color online) The partition of the RGB cube into red and black regions for *Composition with Red and Black* (left). The blank portion of the RGB cube is occupied by pixels from the essentially white background. The partition of the RGB cube into regions occupied by black and background pixels for the Matter painting that resembles *Free Form* is shown to the right. The region of the RGB cube occupied by background pixels is shown in green; by the white layer, left blank. The RGB cube has been sliced to reveal a cutaway. Note how the different colored layers occupy complex interpenetrating regions of RGB color space.

Red and Black into its red and black layers. As discussed above the red pixels and black pixels form irregular interpenetrating swarms in RGB color space. The simplest approach to color separation is to place two nonintersecting spheres inside color space and to count the pixels inside one as red and the ones inside the other as black. The location of the spheres and their size are fitting parameters that can be adjusted to ensure that each sphere encloses as many of the right kind of pixels as possible and as few of the wrong sort. Typically, however either different colors get mixed or parts of a layer get left behind as background residue, as illustrated in Fig. 1 of the paper. Thus this method, which was used in Ref. [9], has few virtues besides ease of implementation. [Parenthetically we note that Fig. 1 in the paper was generated by taking the center of the black sphere at $(R,G,B)=(41,40,41)$ and the red sphere at (161,15,34). The radius of both spheres was taken to be 40. The centers were chosen by using the median (R,G,B) values, as computed using Photoshop, and the radius was optimized by trial and error].

In the Photoshop method the user selects a pixel using a tool called magic wand. All pixels within a narrow user-controlled RGB range (the "tolerance") of the selected pixel are then highlighted by magic wand. If they are all from the desired layer they are transferred to a blank background. The user continues to select pixels in this way until the entire layer has been transferred. By judicious selection of pixels and use of a narrow tolerance accidental selection of pixels from a different layer can be minimized. Schematically the contrast between the simple method of the previous paragraph and the Photoshop method is that the former attempts to enclose the swarm of red pixels within a single well-chosen sphere; the Photoshop method covers it with a series of small spheres and can therefore accommodate the large extent and the irregular shape.

In the adaptive RGB mesh approach the color cube is divided up into eight smaller cubes which are designated with a binary address. 011 for example refers to the subcube where $0<R<127$, $128<G<255$, and $128<B<255$; 101, where $128<R<255$, $0<G<127$, and $128<B<255$; and so forth. The user then examines an image in which only pixels from a single subcube are displayed with their true colors; the other pixels are displayed as white or another user selected uniform background color. If this image is seen to contain pixels from a single layer the user records that the entire subcube contains only pixels of one color. For example, for *Composition with Red and Black* it was found that 001, 010, and 011 contained only black pixels; 100, 101, and 110 contained only red; and 111 contained only background. But if a subcube contains more than one color, as does 000, it is further subdivided into eight cubes and the process is reiterated as many times as needed. *Composition in Red and Black*, for example, required three levels of subdivision. The binary address notation for higher level subdivisions works in the same way. For example the level 2 subcube with binary address 01-10-11 refers to the region where $64<R<127$, $128<G<191$, and $192<B<255$.

The two methods have complementary strengths. The Photoshop method, if skillfully deployed, is faster. Also it allows the user to make better use of spatial information when deciding which pixels to include in a given layer. The adaptive RGB mesh on the other allows for systematic refinement and provides a detailed characterization of the way in which color space is partitioned into the layers of the drip painting. The code we developed to implement RGB mesh included a number of features including the ability to count the pixels in each subcube to determine their relative importance and the ability to regroup and consolidate pixels spatially for easier viewing. In principle the program could be refined to make fuller use of spatial information but in practice we found that results adequate for our needs could be obtained without this feature.

APPENDIX B: DATA

Notes: results obtained using the Photoshop color separation method are marked PS; using adaptive RGB mesh, marked RGB. The known Pollock works are identified by name and their serial number in [21], hereafter abbreviated JPCR. For some paintings the digital image was cropped slightly before analysis. In these cases we give the dimensions of the cropped image used in each analysis. For layers that were force fitted the results are marked ff (see below for a precise description of force fitting). The quantity that is directly inferred from the data is $\ln L_T$ but we present L_T values since it is easier to visualize. However it should be kept in mind that by exponentiating the measured quantity we are amplifying the errors. Thus our two methods agree much better on the location of the box-counting transition than this tabulation of L_T values may suggest. For each painting the results are briefly summarized at the end.

Force fitting. Reference [6] describes a more relaxed procedure called force-fitting that can be applied to paintings that fail to pass the strict authentication test. The procedure is to find the best fit to the data subject to the constraint $L_T>1.0$ cm. Thus authentication criterion (2) is automatically satisfied and authentication is reduced to checking that the other criteria are fulfilled.

1. Untitled 1: (poured media on board). Matter painting that resembles Pollock's *Free Form*.

Physical dimensions: 35.6×44.5 cm

Digital image: 2020×2520 (PS black) 1994×2487 (PS white) 1986×2502 (RGB)

Range of box sizes: 0.2–3.1 cm (PS) 0.2–3.1 cm (RGB)

Black layer:

Area of layer: 43.0% (PS) 38.46% (RGB)

Noise: 0.023 (PS) 0.017 (RGB) 0.020 (RGB ff)

L_T: 1.0 cm (PS) 0.8 cm (RGB) 1.0 cm (RGB ff)

Lower dimension: 1.41 (PS) 1.71 (RGB) 1.73 (RGB ff)

Upper dimension: 1.98 (PS) 1.98 (RGB) 2.00 (RGB ff)

White layer:

Area of layer: 13.9% (PS) 10.86% (RGB)

Noise: 0.024 (PS) 0.023 (RGB) 0.025 (PS ff) 0.024 (RGB ff)

L_T: 0.85 cm (PS) 0.95 cm (RGB) 1.0 cm (PS ff) 1.0 cm (RGB ff)

Lower dimension: 1.47 (PS) 1.35 (RGB) 1.49 (PS ff) 1.36 (RGB ff)

Upper dimension: 1.97 (PS) 1.93 (RGB) 2.00 (PS ff) 1.95 (RGB ff)

Composite layer:

Noise: 0.018 (PS) 0.017 (RGB) 0.021 (PS ff) 0.021 (RGB ff)

L_T: 0.58 cm (PS) 0.59 cm (RGB) 1.0 cm (PS ff) 1.0 cm (RGB ff)

Lower dimension: 1.86 (PS) 1.82 (RGB) 1.90 (PS ff) 1.86 (RGB ff)

Upper dimension: 2.02 (PS) 2.02 (RGB) 2.07 (PS ff) 2.04 (RGB ff)

RGB color partition:

White=111, 010

Black=001, 011, 101,

00-00-01, 00-01-00, 00-01-01,

000-000-000, 000-000-001, 000-001-000, 000-001-001

Brown=100, 110,

01-00-00, 01-00-01, 01-01-00, 01-01-01,

001-000-000, 001-000-001, 001-001-000, 001-001-001

Summary: Satisfies fractal authentication criteria if the more lax force-fitting procedure is allowed.

2. Untitled 14: (poured media on board). Matter painting that resembles Pollock's *Wooden Horse*.

Physical dimensions: 31.7×46.4 cm^2.

Digital image: 1764×2568 pixels

Range of box sizes: 0.2–3.1 cm (PS)

Red layer:

Area of layer: 10.0% (PS)

Noise: 0.014 (PS)

L_T: 1.4 cm (PS)

Lower dimension: 1.36 (PS)

Upper dimension: 1.69 (PS)

Orange layer:

Area of layer: 1.7% (PS)

Noise: 0.024 (PS)

L_T: 0.5 cm (PS)

Lower dimension: 1.28 (PS)

Upper dimension: 0.91 (PS)

Yellow layer:

Area of layer: 5.1% (PS)

Noise: 0.018 (PS)

L_T: 1.2 cm (PS)

Lower dimension: 1.08 (PS)

Upper dimension: 1.69 (PS)

Blue layer:

Area of layer: 4.2% (PS)

Noise: 0.023 (PS)

L_T: 1.0 cm (PS)

Lower dimension: 1.05 (PS)

Upper dimension: 1.67 (PS)

Black layer:

Area of layer: 11.6% (PS)

Noise: 0.014 (PS)

L_T: 1.2 cm (PS)

Lower dimension: 1.36 (PS)

Upper dimension: 1.71 (PS)

White layer:

Area of layer: 11.0% (PS)

Noise: 0.010 (PS)

L_T: 2.0 cm (PS)

Lower dimension: 2.02 (PS)

Upper dimension: 1.81 (PS)

Summary: Does not satisfy fractal authentication criteria. Exhibits anomalous dimensions in orange and white layers.

3. Free Form Pollock (1946) [JPCR 165] (oil on canvas).

Physical dimensions: 48.9×35.5 cm^2

Digital image: 4550×3253 (PS black), 4576×3288 (PS white); 2277×1629 pixels (RGB)

Range of box sizes: 0.1–4.5 cm (PS) 0.2–4.2 cm (RGB)

N.B.: the image was coarsened before RGB analysis to speed up computations. In principle this should have no effect on the fractal analysis since the smallest box sizes exceed the coarsening scale. This expectation is borne out by the concordance between the PS and RGB results.

Black layer:

Area of layer: 56.0% (PS) 54.39% (RGB)

Noise: 0.015 (PS) 0.013 (RGB)

L_T: 1.0 cm (PS) 1.0 cm (RGB)

Lower dimension: 1.79 (PS) 1.85 (RGB)

Upper dimension: 2.05 (PS) 2.02 (RGB)

White layer:

Area of Layer: 20.7% (PS) 23.48% (RGB)

Noise: 0.019 (PS) 0.019 (RGB) 0.021 (PS ff)

L_T: 0.9 cm (PS) 1.0 cm (RGB) 1.0 cm (PS ff)

Lower dimension: 1.57 (PS) 1.60 (RGB) 1.58 (PS ff)

Upper dimension: 2.04 (PS) 2.00 (RGB) 2.06 (PS ff)

Composite layer:

Noise: 0.013 (PS) 0.012 (RGB) 0.012 (RGB ff) 0.015 (PS ff)

L_T: 0.8 cm (PS) 0.65 cm (RGB) 1.2 cm (RGB ff) 1.1 cm (PS ff)

Lower dimension: 1.93 (PS) 1.94 (RGB) 1.96 (RGB ff) 1.93 (PS ff)

Upper dimension: 2.06 (PS) 2.01 (RGB) 2.02 (RGB ff) 2.075 (PS ff)

RGB color partition:

Black=000, 001, 011, 101

Red=100

White=010, 110, 111

Summary: Satisfies fractal authentication criteria if the more lax force-fitting procedure is allowed.

4. The Wooden Horse: Number 10A, 1948 Pollock (1948) [JPCR 207] (oil and enamel paint on canvas).

Physical dimensions: 90.1×190.5 cm^2

Digital image: 2340×1176 (PS and RGB)

Range of box sizes: 0.8–14.2 cm (PS) 0.8–14.0 cm (RGB) 0.8–9.5 cm (RGB, orange layer)

Red layer:

Area of layer: 3.6% (PS) 2.5% (RGB)

Noise: 0.023 (PS) 0.026 (RGB)

L_T: 4.32 cm (PS) 4.32 cm (RGB)

Lower dimension: 1.16 (PS) 1.12 (RGB)

Upper dimension: 1.56 (PS) 1.63 (RGB)

Orange layer:

Area of layer: 1.7% (PS) 1.9% (RGB)

Noise: 0.0301 (PS) 0.027 (RGB)

L_T: 3.23 cm (PS) 2.67 cm (RGB)

Lower dimension: 1.39 (PS) 1.50 (RGB)

Upper dimension: 1.18 (PS) 1.25 (RGB)

Yellow layer:

Area of layer: 1.2% (PS) 1.3% (RGB)

Noise: 0.026 (PS) 0.018 (RGB)

L_T: 7.63 cm (PS) 1.67 cm (RGB)

Lower dimension: 1.11 (PS) 1.26 (RGB)
Upper dimension: 1.05 (PS) 1.08 (RGB)
Black and blue layers:
Area of layer: 10.3% (PS) 2.3% (blue, RGB) 7.4% (black, RGB)
Noise: 0.028 (PS) 0.024 (black RGB) 0.025 (blue RGB)
L_T: 3.91 cm (PS) 4.32 cm (black RGB) 4.32 cm (blue RGB)
Lower dimension: 1.44 (PS) 1.35 (black RGB) 1.14 (blue RGB)
Upper dimension: 1.92 (PS) 1.79 (black RGB) 1.73 (blue RGB)
White layer:
Area of layer: 5.5% (PS) 9.1%
Noise: 0.031 (PS) 0.026 (PS, trimmed range) 0.026 (RGB)
L_T: 3.91 cm (PS) 3.91 cm (RGB)
Lower dimension: 1.30 (PS) 1.39 (RGB)
Upper dimension: 1.82 (PS) 1.86 (RGB)
RGB color partition:
Blue=001, 011,
00-00-01, 00-01-01, 01-00-01,
010-010-011, 010-011-010, 010-011-011, 011-010-011, 011-011-011
0100-0100-0101, 0100-0101-0101, 0101-0100-0101
Black=010,
00-00-00, 00-01-00, 01-00-00,
010-010-001
0100-0100-0100, 0100-0101-0100, 0101-0100-0100, 0101-0101-0100,
0101-0101-0101
Red=101,
10-00-00, 10-00-01, 10-01-00, 11-00-00, 11-01-00, 11-01-01
111-100-011
White=111
Brown=10-01-01, 10-10-01
011-010-001, 011-011-001
011-010-010, 011-011-010
110-100-010, 110-100-011,
Yellow and orange=10-10-00, 11-10-00, 11-11-00, 11-11-01
110-101-010, 110-101-011, 111-100-010, 111-101-010, 111-101-011

Notes: in the PS analysis the blue and black layers were analyzed as a composite. In the RGB analysis the horse's head was not fully excluded from the white layer; thus, the PS analysis of the white layer is more accurate. The yellow and orange layers in the RGB analysis were separated by incorporating spatial information. If the pixels lay in the appropriate region of RGB and real space they were deemed yellow; otherwise orange.

Summary: Does not satisfy fractal authentication criteria. Exhibits anomalous dimensions in the orange and yellow layers.

5. Untitled: Pollock (1950) [JPCR 797] (enamel on paper).

Physical dimensions: 28.3×150.3 cm^2
Digital images: 1145×5150 pixels (PS and RGB) 1145×2908 (RGB-cropped).
Range of box sizes: 0.1–2.7 cm (PS) 0.1–4.4 cm (RGB) 0.1–3.0 cm (RGB-cropped)
Black layer:
Area of layer: 5% (PS) 5% (RGB)
Noise: 0.020 (PS) 0.024 (RGB) 0.024 (RGB-cropped)
L_T: 0.5 cm (PS) 0.5 cm (RGB) 0.5 cm (RGB-cropped)
Lower dimension: 1.73 (PS) 1.72 (RGB) 1.72 (RGB-cropped)
Upper dimension: 1.36 (PS) 1.37 (RGB) 1.39 (RGB-cropped)
RGB color partition:
Black=000

Summary: Does not satisfy fractal authentication criteria. Exhibits anomalous dimensions.

6. Number 8, 2007: Ash and Hallen (2007) (oil on canvas).

Physical dimensions: 122×152 cm^2 (approximately)
Digital image: 1387×1668 pixels (PS) 1192×1566 pixels (RGB)
Range of box sizes: 0.9–15.3 cm (PS) 0.3–6.0 cm (RGB)
Black layer:
Area of layer: 44.0% (PS) 58.3% (RGB)
Noise: 0.014 (PS) 0.022 (RGB)
L_T: 3.8 cm (PS) 1.6 cm (RGB)
Lower dimension: 1.89 (PS) 1.81 (RGB)
Upper dimension: 2.08 (PS) 2.05 (RGB)
RGB color partition:
Black=000, 001, 010, 011, 100, 101, 110
Background=111

Comments: the discrepancy between the percentage area of black obtained by the two color separation methods is due to the different ways the painting was cropped before color separation. The cropped image used in the Photoshop analysis contained a margin that was largely white. The discrepancy between the L_T values is presumably due to the same cause.

Summary: Satisfies fractal authentication criteria.

7. Composition with Red and Black: Ash and Hallen (2007) (oil on canvas).

Physical dimensions: 122×152 cm^2 (approximately)
Digital image: 1288×1536 pixels
Range of box sizes: (PS) 0.3–16.4 cm (RGB)
Black layer:
Area of layer: 33.4% (PS) 37.2% (RGB)
Noise: 0.023 (PS) 0.021 (RGB)
L_T: 1.75 cm (PS) 1.75 cm (RGB)
Lower dimension: 1.68 (PS) 1.64 (RGB)
Upper dimension: 2.02 (PS) 2.01 (RGB)
Red layer:
Area of layer: 17.0% (PS) 22.3% (RGB)
Noise: 0.020 (PS) 0.025 (RGB)
L_T: 4.13 cm (PS) 1.59 cm (RGB)
Lower dimension: 1.48 (PS) 1.48 (RGB)
Upper dimension: 2.01 (PS) 1.98 (RGB)
RGB color partition:
Black=001, 010, 011,
00-00-00, 00-00-01, 00-01-00, 00-01-01, 01-01-00, 01-01-01
Red=100, 101, 110,
01-00-00, 01-00-01

FIG. 6. (Color online) Pollock and Matter Paintings I. Top, Jackson Pollock, *The Wooden Horse Number 10A, 1948* (1948) and bottom, *Untitled 14* (artist unknown). Both paintings fail to satisfy the fractal authentication criteria by having two of their six color layers with $D_D > D_L$. Thus, according to fractal analysis, *The Wooden Horse*, an undisputed Pollock painting, fails to be authentic. Pollock images are reproduced by permission ©2009 The Pollock-Krasner Foundation/Artists Right Society (ARS), New York. Reproduction, including downloading of Pollocks works is prohibited by copyright laws and international conventions without the express written permission of ARS, New York.

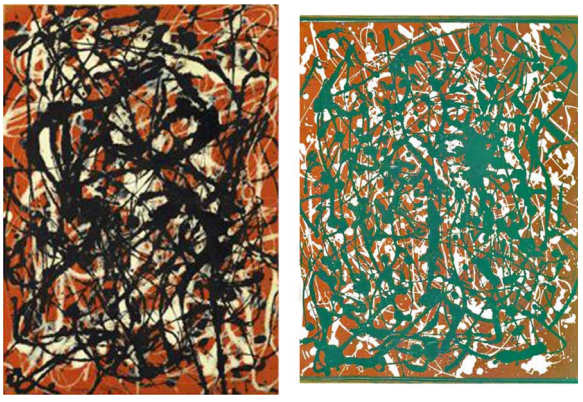

FIG. 7. (Color online) Pollock and Matter Paintings II. Left, Jackson Pollock, *Free Form (1946)* and right, *Untitled 1* (artist unknown). Both paintings pass the fractal authentication criteria provided some force fitting is allowed. Thus, contrary to the findings of Taylor *et al.* [1], we find at least one Matter painting (i.e., *Untitled 1*) that satisfies the fractal authentication criteria. Pollock images are reproduced by permission ©2009 The Pollock-Krasner Foundation/Artists Right Society (ARS), New York. Reproduction, including downloading of Pollocks works is prohibited by copyright laws and international conventions without the express written permission of ARS, New York.

FIG. 8. (Color online) Paintings by Ash and Hallen. *Number 8, 2007* (2007) (top left), *Composition with Red and Black* (2007) (top right), and detail from *Untitled* (2007) (bottom). Three paintings from a series of nine, two of which (*Number 8, 2007* and *Composition with Red and Black*) have been analyzed and found to satisfy the fractal authentication criteria used to identify Pollock paintings. All paintings are oil on canvas.

Background=111
Summary: Satisfies fractal authentication criteria.

APPENDIX C: ART GALLERY

In Figs. 6–9 we present a gallery of paintings and drawings discussed in this paper.

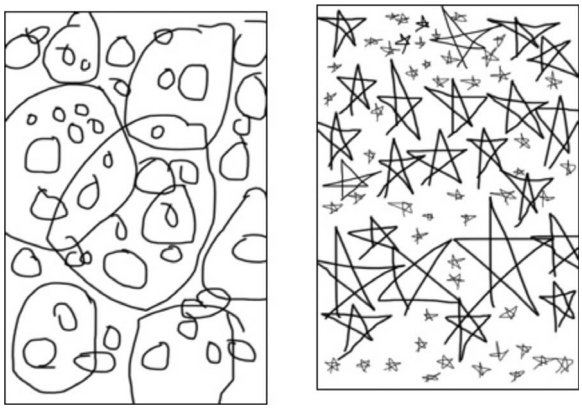

FIG. 9. Sketches *Gross Pebbles* (left) and *Mixed Stars* (right) by Katherine Jones-Smith (2006). Like *Untitled 5* [7], these crude drawings satisfy the fractal authentication criteria used to identify Pollock, although they are indisputably not works by Pollock. These freehand drawings were created using Adobe Photoshop as described in Ref. [7].

[1] A. Abbott, Nature (London) **439**, 648 (2006).
[2] R. P. Taylor, A. P. Micolich, and D. Jonas, Nature (London) **399**, 422 (1999).
[3] R. P. Taylor, A. P. Micolich, and D. Jonas, Phys. World **12**, 15 (1999).
[4] R. P. Taylor, A. P. Micolich, and D. Jonas, Leonardo **35**, 203 (2002).
[5] R. P. Taylor, in *Art and Complexity*, edited by J. Casti and A. Karlqvist (Elsevier, Amsterdam, 2003), p. 117.
[6] R. P. Taylor, R. Guzman, T. P. Martin, G. D. R. Hall, A. P. Micolich, D. Jonas, B. C. Scannell, M. S. Fairbanks, and C. A. Marlow, Pattern Recognit. Lett. **28**, 695 (2007).
[7] K. Jones-Smith and H. Mathur, Nature (London) **444**, E9(2006).
[8] J.-F. Muzy, Ann. Phys. (Paris) **20**, 63 (1995).
[9] J. R. Mureika, C. C. Dyer, and G. C. Cupchik, Phys. Rev. E **72**, 046101 (2005); J. R. Mureika, Chaos **15**, 043702 (2005), discusses some of the limitations of various color separation methods.
[10] Unfortunately Taylor *et al.* [2–6] nowhere provided sufficient information about their color separation method to allow us to calibrate our techniques against theirs.
[11] It appears on the list of 17 paintings that were the basis of the criteria in a preprint version of Ref. [6] but not in the published version.
[12] D. Anfam, S. Davidson, and M. Ellis, *No Limits, Just Edges: Jackson Pollock Paintings on Paper* (Guggenheim Museum, New York, 2005).
[13] Our box counter uses the round-off rule that a pixel occupies a box if more than half the area of the pixel lies inside the box. It places the origin of the grid of boxes at the lower left corner of the canvas; boxes on the top and right edges that lie partly outside the canvas are not counted. We have explored other common variations such as including pixels in a box if they intersect it at all, treating the edge boxes on the same footing as the interior boxes, and offset averaging, where we shift the origin of our box grid and average over different locations. We have verified that all these alternatives lead to essentially the same results.
[14] K. Jones-Smith, H. Mathur, and L. M. Krauss, e-print arXiv:0803.0530.
[15] G. H. Hardy and E. M. Wright, *An Introduction to the Theory of Numbers* (Oxford University Press, Oxford, 1979).
[16] M. L. Mehta, *Random Matrices* (Academic, San Diego, 1991).
[17] M. F. Barnsley, *Fractals Everywhere*, 2nd ed. (Academic, Boston, 1993).
[18] W. H. Press, S. A. Teukolsky, W. T. Vetterling, and B. P. Flannery, *Numerical Recipes*, 2nd ed. (Cambridge University Press, Cambridge, England, 1992).
[19] E. Ott, *Chaos in Dynamical Systems* (Cambridge University Press, Cambridge, England, 2002).
[20] For an early interpretatin of multifractals as an admixture of fractals, see U. Frisch and G. Parisi, in *Turbulence and Predictability in Geophysical Fluid Dynamics and Climate Dynamics*, edited by M. Ghil, R. Benzi, and G. Parisi (North-Holland, Amsterdam, 1983), pp. 84–87.
[21] F. V. O'Connor and E. V. Thaw, *Jackson Pollock: A Catalogue Raisonné of Paintings, Drawings and Other Works* (Yale University Press, New Haven, 1978).